Copper enrichment on aluminium surfaces after electropolishing and its effect on electron imaging and diffraction

Sigurd Wenner [a,b,*], Adrian Lervik [b], Elisabeth Thronsen [b], Calin D. Marioara [a], Stephan Kubowicz [a], Randi Holmestad [b]

[a] SINTEF Industry, Postboks 4760, Torgarden, Trondheim 7465, Norway
[b] Department of Physics, Norwegian University of Science and Technology (NTNU), Trondheim 7491, Norway

ARTICLE INFO

ABSTRACT

Electropolishing is the most common method of preparing samples of aluminium alloys for scanning and transmission electron microscopy, as it yields a good surface quality and large flat, electron-transparent areas. Like many chemical surface treatment procedures, the electropolishing process can create a Cu-rich layer between the aluminium matrix and the outermost aluminium oxide layer. The Cu layer is shown to be crystalline, which causes several distinct effects on electron images and diffraction patterns, that can easily be misinterpreted as originating from features inside the aluminium matrix. The layer is a modified θ'–Al$_2$Cu phase, with a semi-coherent interface with aluminium. A θ' superstructure suggested in this paper can explain lattice modulations with a 1 nm spacing that have been observed in the [011]$_{Al}$ zone axis of electropolished specimens. Evidence of Cu diffusion into the Al matrix was also found. The surface enrichment can also occur in Cu-free aluminium alloys, as small amounts of Cu can be introduced from outside sources through the electrolyte solution.

1. Introduction

In all forms of electron microscopy and spectroscopy, the surface quality of the specimen is vital to the success of an experiment. In the case of high resolution (scanning) transmission electron microscopy ((S) TEM), some common unwanted surface features are: (i) oxides produced during specimen preparation or subsequent exposure to air [1,2], (ii) elemental segregation layers [3,4], (iii) amorphized, or otherwise damaged layers due to ion beam preparation [5–7], and (iv) hydrocarbon or other volatile contamination [8–10]. Typically, (iv) can be identified through temporal intensity variations and (iii) through spatial intensity variations. Meanwhile, (i) can be either smooth or rough, amorphous or (nano-)crystalline, and may have a very different chemical composition from the bulk of the specimen. Similarly, (ii) can be either randomly distributed or ordered, and compositions of features in the specimen can be difficult to determine if the whole specimen is covered in a segregated surface layer.

Smooth, high quality surfaces and thin foils of metallic alloys can be easily prepared by electropolishing [11–13]. The crystal structures in the specimen are usually well preserved by the process, except in cases where phases in the material reacts differently to electropolishing,

causing preferential etching, selective dissolution or rapid oxidation. The preparation can in principle be done using a simple home-made setup and does not need expensive equipment such as an ion milling system. For these reasons, electropolishing is by far the most commonly used method to prepare thin foils of aluminium alloys for both routine and high-end (S)TEM investigation of precipitate phases [14–22].

However, electropolished TEM specimens of copper-containing aluminium alloys are often host to a copper-rich crystalline surface layer, which is situated below the aluminium oxide [23,24]. A similar layer is produced by exposure to an acidic or alkaline solution with no current applied [25]. Such a Cu-rich layer has a subtle electron scattering signature that may lead to false interpretations about properties of the bulk material.

As will be demonstrated in this paper, a Cu-containing surface layer can also form while electropolishing a nominally Cu-free alloy with a methanol/nitric acid mixture. We explore the origin of the Cu layer, the chemical and structural characteristics of the layer and how it affects data obtained from transmission electron microscopy and, in particular, electron diffraction experiments.

---

* Corresponding author at: SINTEF Industry, Postboks 4760 Torgarden, 7465, Trondheim, Norway
E-mail address: sigurd.wenner@sintef.no (S. Wenner).

2. Methods

Two alloys were selected for this study: (i) Alloy 1, an Al-Zn-Mg alloy containing a very low amount of Cu (the lowest amount obtainable in large volume industrial production). (ii) Alloy 2, an Al-Mg-Si-Cu alloy containing a moderate amount of Cu for easy observation of the artifacts introduced in TEM imaging and diffraction. The composition of the alloys is shown in Table 1. Alloy 1 was extruded, water cooled and stored at room temperature for 17 years. Alloy 2 was rolled to a 2 mm plate, given a solution heat treatment at 550 °C for 5 min, water quenched, and given a pre-aging treatment at 90 °C for 24 h. Both materials were produced for the study of clustering during low-temperature aging of aluminium alloys, which demands a very high specimen quality to discern subtle clustering and ordering phenomena from images and diffraction patterns.

2.1. TEM sample preparation

Specimens were mechanically polished to discs of thicknesses around 80 μm and electropolished using a common electrolyte consisting of 1/3 nitric acid in 2/3 methanol, cooled to −25 °C. A Tenupol-5 twin-jet electropolisher (Struers Inc., Cleveland, OH, USA) was used with an applied voltage of 20 V. Alloy 1 was electropolished with a brand new Tenupol-5 unit and a freshly prepared electrolyte for optimum cleanliness. After electropolishing, the specimens were immersed twice in methanol and twice in ethanol before being left to dry on filter paper.

Cross-sections of electropolished specimens were produced by the focused ion beam (FIB) lift-out method, using a FEI Helios G4 UX dual-beam instrument (Thermo Fisher Scientific, Waltham, MA, USA). The specimens were coated with carbon (electron- and ion-deposited) prior to FIB lift-out, and the final thinning was done with 2 kV Ga^+ ions to optimize the surface quality.

2.2. Analysis of electrolyte solutions

An electrolyte for TEM specimen preparation is typically reused several times for many specimens of different alloy compositions. It is therefore interesting to analyze the chemistry of the electrolyte, as it is reasonable to assume that elements dissolved into the electrolyte from one specimen can transfer onto the surface of succeeding specimens. The electrolyte was prepared with 65% Suprapur® nitric acid and ≥99.9% EMSURE® methanol, both supplied by Merck KGaA. 1.5 L of fresh electrolyte (used to prepare alloy 1) was mixed into a new glass bottle using a plastic funnel and glass measuring beaker. A sample of 10 ml was extracted. A corresponding sample was collected from an old electrolyte, used to prepare a variety of aluminium alloy specimens for 3 months.

The metallic ions dissolved in the electrolytes and their ingredient chemicals were measured with inductively coupled plasma mass spectroscopy (ICPMS) using an Agilent 8800 Triple Quadrupole instrument. The concentrations were quantified against standards from Inorganic Ventures and using ^{115}In as an internal standard.

2.3. Surface chemistry of TEM specimens

Time-of-flight secondary ion mass spectrometry (ToF-SIMS) analysis was performed on an as-prepared TEM sample of alloy 1 using a 'TRIFT V nanoTOF' instrument (Physical Electronics, Chanhassen, MN, USA) equipped with a 30 kV Ga^+ source for analysis and an O_2^+ source for sputtering. The bunched, primary Ga^+ ion beam was scanned over an area of 100 μm × 100 μm under static conditions (total ion dose < 1 × 10^{12} ions/cm^2). All ejected positive secondary ions from the surface were collected for analysis. Since the sample is conductive, no charge compensation was required. The mass scale of the positive ion spectrum was calibrated using the Na^+, Cu^+, and Ga^+ peaks before further analysis.

For depth profiling an O_2^+ ion beam with 3 keV energy was rastered over a 600 μm × 600 μm area. Depth profiles of various elements were obtained at room temperature by alternately recording a mass spectrum and then sputtering the area for 10 s. The sputtering depth could not be measured accurately due to the uneven sample surface.

In cases where the bulk concentration of an element was determined by ICPOES (see Table 1), the relative sensitivity factor (RSF) for these elements in the Al matrix could be calculated from the ion intensities of the respective elements. The RSF is a measure for the different ionization probabilities of different elements in a certain matrix and is needed for reliable quantitative analysis.

2.4. STEM and EELS

Annular dark-field (ADF)-STEM imaging and spectroscopy were conducted with a probe/image aberration corrected JEOL ARM-200CF cold field emission gun microscope (JEOL Ltd., Tokyo, Japan). It was operated at 200 kV during conventional plan-view imaging, and 80 kV during imaging of cross-sectional specimens, to limit damage to the surface layers. The convergence angle of the beam was 27 mrad and the ADF-STEM collection angles were 67–118 mrad. Electron energy loss spectroscopy (EELS) was performed with a Gatan image filter (GIF) Quantum. The outer EELS collection angle was 67 mrad and the dispersion was 0.4 eV/channel. A power-law background was subtracted from spectra before core loss edges were integrated to form a depth profile of elemental concentration.

Diffraction patterns were simulated kinematically using the CrystalKit software.

3. Results

3.1. Electrolyte composition

Table 2 gives the measured composition of the electrolyte. All metallic ions that we expect to find within aluminium alloys, as well as the common contaminant Ca, have a higher concentration in the old electrolyte than in the new one. The Al content rises sharply with use of the electrolyte, as expected, and the 128 mg in the 1.5 L of mixture corresponds to about 80 full TEM specimen discs (weighing 1.5 mg each). The electrolyte has been used to prepare hundreds of specimens, but only a fraction of their volumes was polished away. Some of the metallic ions may also have agglomerated as small particles in the bottom of the electrolyte container and were therefore not included in ICPMS measurements. The high amount of Fe in the old electrolyte probably comes from steel components such as electrical contacts in the electropolishing unit.

The surprising result here is that the increase in Cu content is not drastic after usage; the concentration of Cu is high already in the newly mixed (unused) electrolyte. While the chemicals by themselves did not contain Cu, after being in contact with a funnel and a measuring beaker, mixed and stored in a new glass bottle, the amount of Cu in the 1.5 L of

Table 1

Composition of the alloys in weight%. Alloy 1 was measured by inductively coupled plasma optical emission spectroscopy (ICPOES), while the nominal composition is given for alloy 2.

	Fe	Si	Mg	Mn	Cr	Cu	Zn	Ti	Zr
Alloy 1	0.165	0.082	1.233	0.004	0.001	0.019	6.92	0.013	0.162
Alloy 2	0.15	0.85	0.70	0.25	–	0.60	–	–	–

Table 2
ICPMS measurements of metallic ions in two different electrolyte batches and in the initial ingredients used to prepare the electrolytes. Numbers are in μg/L.

Sample	Mg	Al	Ca	Cr	Mn	Fe	Ni	Cu	Zn
Old electrolyte	1392	85,280	6969	2938	432	11,199	2211	2437	762
Fresh electrolyte	92	336	2155	22	47	190	15	1355	45
Nitric acid	67	68	195	1	0	18	2	1	8
Methanol	17	21	151	6	<5	8	<5	<5	9

mixture was about 2 mg. There is a similar increase of Ca, and slight increases in all other elements, after mixing.

3.2. Surface chemistry of TEM specimens

ToF-SIMS depth profiling was conducted on TEM specimens of alloy 1. The concentration of alloying elements as function of the sputter time could be determined quantitatively at each measuring point by using the calculated RSFs (Fig. 1a). For other detected elements where the bulk concentration was not determined, relative changes in the amount of an element as a function of depth are shown by the count ratio between the element of interest and aluminium (Fig. 1b). For these calculations the Al_2 peak intensity was used as matrix value because the Al peak intensity was very high, which most likely caused detector saturation and thus a non-linearity in the count rate. The figures show that elements Mg, Si, Cu, and Ni are enriched near the electropolished surface, with Cu having the largest relative increase. The common contaminants Ca, Na and CH_3 are also present at the surface. Meanwhile, the elements Fe, Zn, Ti and B are depleted near the surface.

Since the depth profile is averaged over a large, uneven area, the depth resolution is limited and it is not easy to separate features of the upper matrix, oxide layer, and deposits on the surface. On the other hand, the low detection levels allow for measurement of trace elements such as Ti and B, which are added to the alloy for grain refinement [26]. Glow-discharge optical emission spectroscopy (GD-OES) have been used to pinpoint the presence of the Cu-rich film below the aluminium oxide [27,28], at the expense of detection limit and number of measured elements. The composition gradients stabilize after a sputtering time of about 350 s, presumable corresponding to a few tens of nanometers.

3.3. TEM observations of the Cu-rich layer

Crystalline Cu-rich layers were observed by TEM in both alloys. We focus on the TEM results from alloy 2 which contains the highest amount of Cu. Fig. 2 shows ADF-STEM images and electron diffraction patterns from grains with surface normals parallel to the $[001]_{Al}$ and $[011]_{Al}$ directions. A few crystallographic features exist that differentiate the specimen from a perfect aluminium lattice:

1. The forbidden {110} diffraction spots are present in both the Fourier transform of the ADF-STEM image (Fig. 2b) and the selected-area diffraction pattern obtained in the [001] projection (Fig. 2c).
2. Four spots, indicated by yellow circles, in Fig. 2c are visible around the forbidden {110} spots in the diffraction pattern, and sometimes also visible in the STEM Fourier transform. These are only seen in early stages of aging, and are associated with Frank-Kasper ordering during clustering of solute atoms [29,30].
3. Satellite spots around the direct beam and main Al diffraction spots are seen in both the STEM Fourier transform and diffraction pattern in the [001] projection, Fig. 2e-f. These indicate a periodicity of about 1.0 nm along the $\left[0\bar{1}1\right]$ direction, corresponding to 7 times the $\left(0\bar{2}2\right)$ plane spacing. This phenomenon is visible in the STEM image as a horizontal intensity modulation. The stripes are not scanning artifacts, as they appear irrespective of dwell time, image rotation and magnification.

In order to explain point 3, we prepared cross-sectional FIB lamellae from the electropolished TEM specimens, originating from the same grain and oriented along the horizontal (100) planes and vertical $\left(0\bar{1}1\right)$ planes in Fig. 2d. Point 1 will also be addressed in the FIB-TEM analysis.

Fig. 3 shows STEM images from the bulk region of the two cross-sectional FIB specimens, to be compared with Fig. 2. The specimen thicknesses are about 20 nm, as measured by EELS. Bearing in mind that microscopy parameters are not identical (e.g. the voltage was reduced from 200 to 80 kV), the image quality is roughly similar for the two preparation methods. The reason for showing these images is to point out that the extra diffraction spots mentioned above are not seen in the bulk of the FIB prepared specimen. They must therefore originate from features belonging to the surfaces of the electropolished specimen.
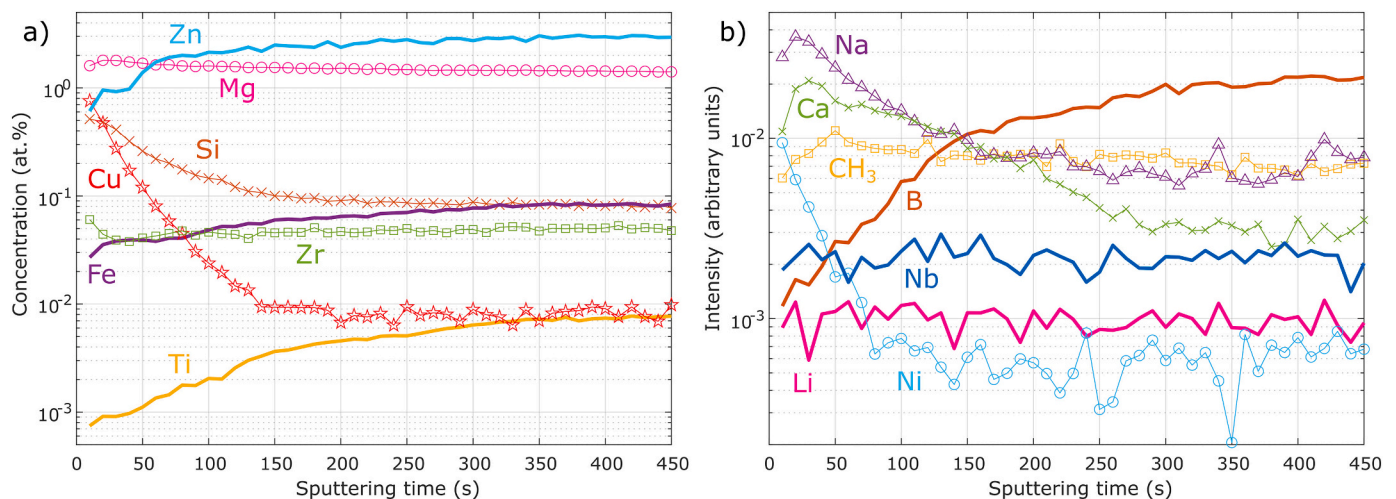

Fig. 1. ToF-SIMS depth profile from an electropolished specimen of alloy 1. a) Concentration of alloying elements normalized by bulk compositions measured using ICPOES (Table 1). b) Signal intensity of other elements.
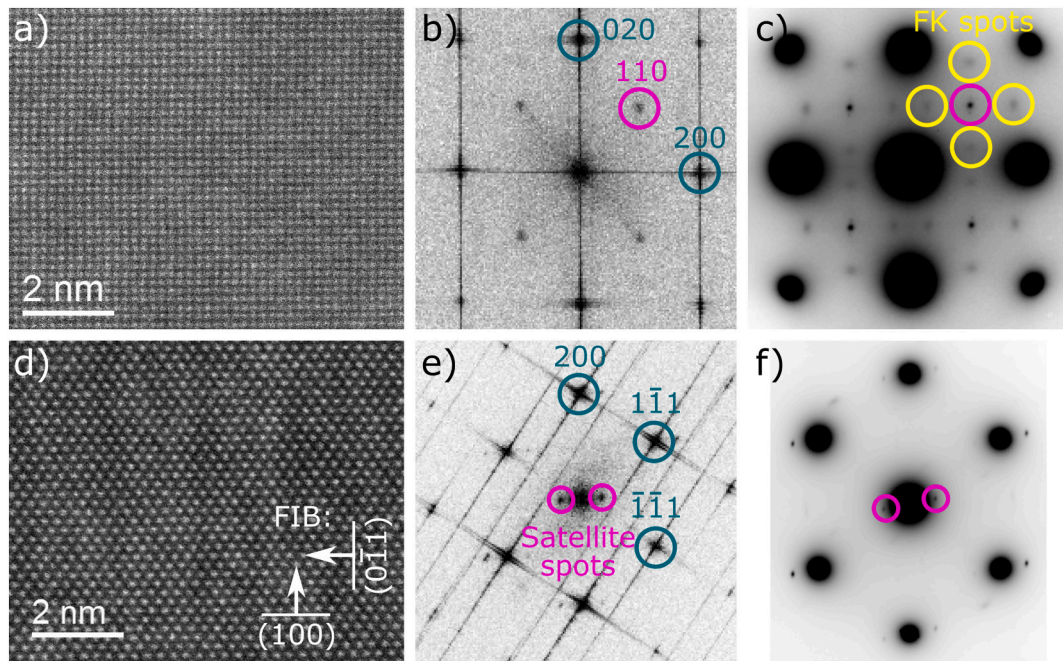
Fig. 2. TEM results from an electropolished specimen of alloy 2, acquired with 200 kV electrons. a,d) Cutouts from larger ADF-STEM images in the [001] and [011] projections, respectively. The planes for the FIB prepared cross-sections are indicated. b,e) Corresponding Fourier transforms. c,f) Selected-area diffraction patterns from the same grains as a,d).
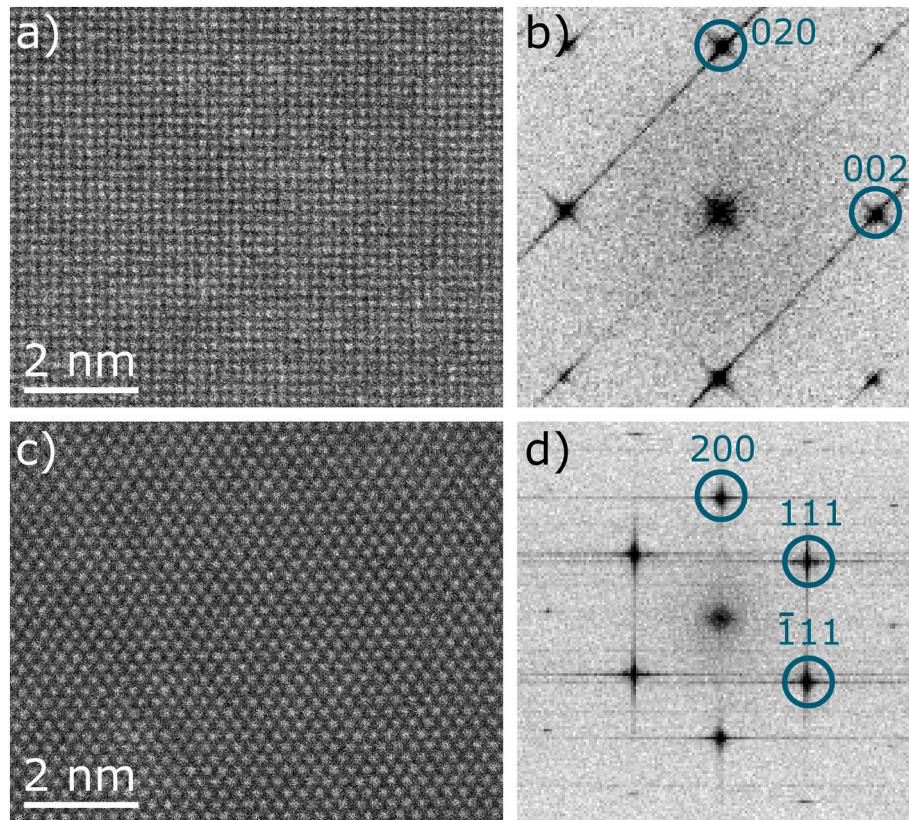

Fig. 3. Cutouts from ADF-STEM images from the FIB specimen of alloy 2, acquired with 80 kV electrons. The imaged areas are approx. 150 nm below the electropolished surface. a) [100] projection, c) $\left[0\bar{1}1\right]$ projection and b,d) corresponding Fourier transforms. None of the extra diffraction spots observed in Fig. 2 are visible.
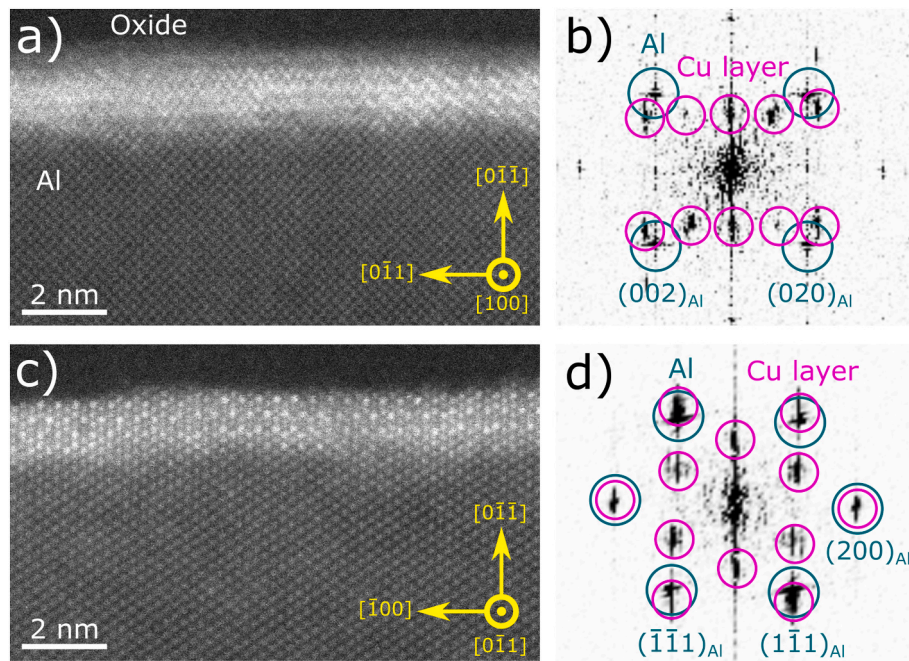
Fig. 4. ADF-STEM images from the cross-section of an electropolished specimen of alloy 2, acquired with 80 kV electrons. The images are projected in the a) [100] direction and b) $\left[0\bar{1}1\right]$ direction. b,d) show corresponding Fourier transforms.

Moving upwards from the bulk, Fig. 4 shows ADF-STEM images from the cross-section of the electropolished surface. A bright, crystalline layer with a thickness of approx. 1.5 nm is apparent below the amorphous aluminium oxide at the surface. The Fourier transforms show that the interface is coherent along the $[100]_{Al}$ direction, but not along the $\left[0\bar{1}1\right]_{Al}$ direction. Since the surface is not completely parallel to the $(011)_{Al}$ plane, the interface is stepped in the $\left[0\bar{1}1\right]_{Al}$ projection, which is why it appears blurry in the $[100]_{Al}$ projection.

Image modes that shows strain contrast reveal interface dislocations in the [100] projection. Fig. 5 shows a bright-field TEM image of the interface, acquired with an objective aperture large enough to keep the Al lattice resolved. Dislocations appear quite regularly, which means that the interface is semi-coherent. The spacing between dislocations is about 2.0 nm, which corresponds to $7 \times (011)_{Al}$ planes. One might think that the periodic dislocations produce the intensity modulation observed with the electron beam through the electropolished specimen (see Fig. 2d). However, the intensity modulation has a halved spacing of 1.0 nm, as shown in the inset of Fig. 5. This discrepancy will be addressed in the discussion section.

EELS was used to obtain chemical information from the Cu-rich layer. A spectrum image was obtained in the $\left[0\bar{1}1\right]_{Al}$ projection as the interface of the Cu-containing layer with the Al matrix is most parallel to this direction. Fig. 6a shows a concentration profile from the surface and into the alloy matrix. The aluminium oxide layer at the top and the Cu-rich surface layer below seem clearly separated. In addition, there is a region in the matrix below the surface layer extending approximately 5 nm, where the Cu concentration is somewhat higher than in the bulk matrix. Fig. 6c shows a summed Fourier transform of the matrix region in Fig. 4a, which is within the Cu-enriched zone. Contrary to the bulk (see Fig. 3a-b), the near-surface region does exhibit the forbidden {110} spots.

The EELS signal from the Cu-rich layer was integrated and is shown in Fig. 6d, zoomed in on the Cu-$L_{2,3}$ core loss edge. The signal should be gradually increasing for metallic Cu, and have sharp peaks (white lines) for Cu oxides with molecular bonds [31]. The spectrum in Fig. 6d represents a mixture between these cases. The white lines appear with equal strength all through the layer, which rules out that the lines come exclusively from bonding to the oxide layer on the top. A more likely explanation is that the Cu-rich layer is characterized by a mixture of metallic and covalent/ionic bonds.
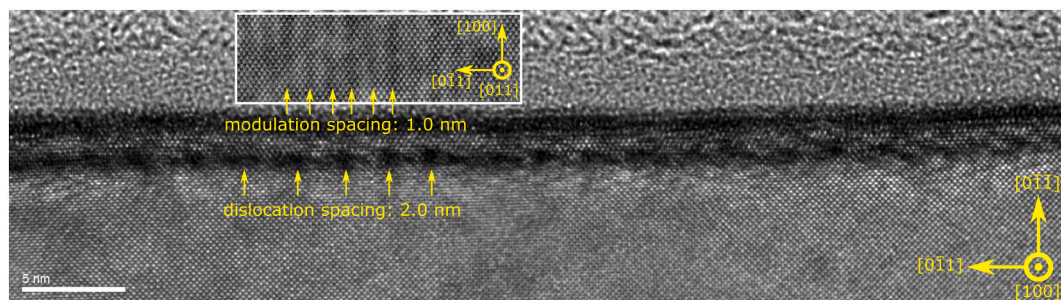

Fig. 5. Bright-field TEM image from the cross-section of an electropolished specimen of alloy 2, acquired with 80 kV electrons. The image is projected in the [100] direction. The inset shows a plan-view ADF-STEM image from the electropolished specimen (similar to Fig. 2d).
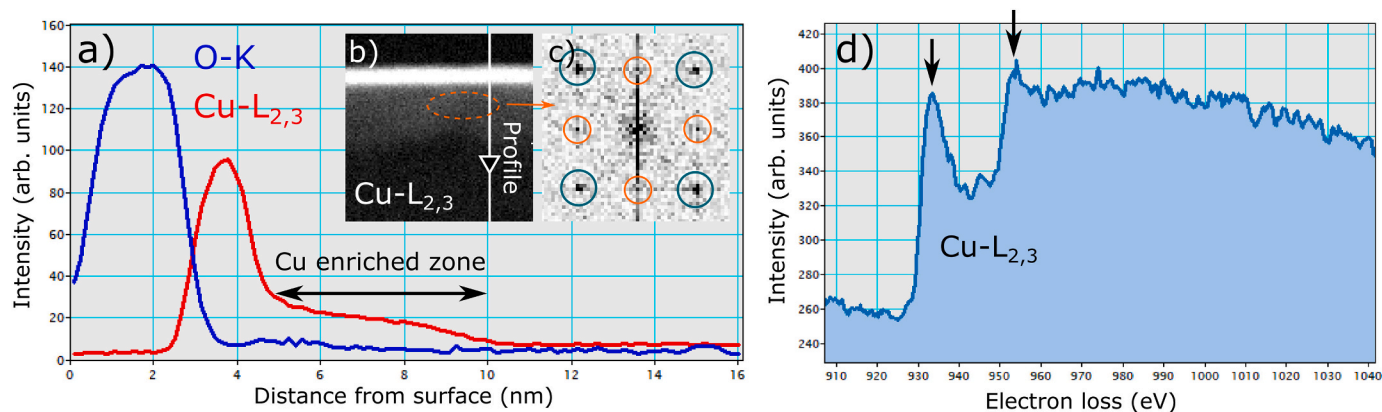
Fig. 6. a) Concentration of O and Cu through the surface layers of alloy 2. The insets show b) the original EELS image, acquired from the [110] projection at 80 kV and c) a Fourier transform from the Cu enriched zone in Fig. 4a. d) shows the Cu-L$_{2,3}$ core loss edge integrated through the Cu-rich layer. The arrows point to the molecular white lines.

4. Discussion

4.1. Cu layer – Origin

The freshly prepared electrolyte contained 1355 µg/L Cu. The Cu was confirmed not to originate from the nitric acid or methanol, so it is likely that it was picked up from the surfaces of the funnel or the beaker used for measuring the chemicals. This equipment is typically washed with tap water that goes through copper pipes. Cu ions are absorbed in the water, in an amount depending heavily on the state of corrosion in the pipes and the time the water has spent inside the pipes [32]. Further, the equipment is air-dried, which allows Cu deposits to form. Cu ions are easily dissolved in nitric acid [33], which means all the deposited Cu from the tap water end up in the electrolyte. The electropolishing unit and its container are also cleaned with tap water, which can introduce more Cu and other contaminants, since the electrolyte is replaced in the container upon re-use. Our hypothesis is therefore that the Cu ions present in the electrolyte mainly originates from tap water, and not from aluminium alloy specimens. The local drinking water is soft, but some Ca is always to be expected, which explains why there is also a high concentration of Ca in the electrolyte.

The ToF-SIMS depth profile of an (almost) Cu-free alloy electropolished with the fresh electrolyte uncovered a surface enrichment of Mg, Si, Cu and Ni, and corresponding depletion of Fe, Zn, Ti and B (see Fig. 1). Since some elements are being depleted in the matrix near the surface, significant dealloying/dissolution into the electrolyte must be occurring, and not simply deposition of ions contained in the electrolyte onto the surface. Focusing on Cu, this leaves two possible explanations for the surface enrichment, namely: (i) Cu originates from the electrolyte or (ii) Cu is up-concentrated from the dilute solid solution in the alloy matrix while Al and other elements are consumed.

Assuming a θ'–Al$_2$Cu structure (see next section), ballpark calculations can estimate that both mechanisms for surface enrichment are possible. A circular area with diameter of about 2 mm is electropolished on each specimen. A 1.5 nm thick θ' layer covering the surfaces on both sides requires 0.02 ng of Cu. By comparison, 1 µL (1 mm^3) of our fresh electrolyte contains 1.4 ng Cu, a 70 times higher amount. It is plausible that the specimen encounters enough solution and that the applied voltage provides enough driving force for the Cu atoms to precipitate onto the surface, in a process similar to electroplating [34]. In this case the layer must move continuously inwards during the 1–2 min the process takes, while Al and other atoms diffuse past it and become dissolved in the electrolyte.

If the θ' layer is formed exclusively by selective dealloying, the Cu inside the layer (33.3 at.%) must have been up-concentrated from the matrix (0.0081 at.% for alloy 1), giving a concentration ratio of about

4000. Assuming a 1.5 nm thick Cu layer in alloy 1 (as was measured in alloy 2), the Cu must have come from a 6 µm depth of matrix, which is plausible, since there is about 40 µm of matrix to take from on each side of an 80 µm thick specimen.

The reality is probably a complicated interaction between specimen and electrolyte, and a combination of the two mechanisms occurring. In any case, Cu ions are easily dissolved by the nitric acid/methanol electrolyte and is shown to have a very high affinity to the aluminium surface.

The spectroscopy results in Fig. 6 teach us two things: (i) The Cu-rich surface layer is not an oxide, but is rather placed below a thicker layer of amorphous Al oxide. The oxide layer is assumed to form when the specimen comes out of the electrolyte and into air, by Al atoms diffusing through the Cu-rich layer. (ii) There is a region of fcc-Al matrix below the surface layer which is enriched in Cu. Similarly, a Cu-rich surface layer with a Cu-enriched matrix zone below was measured on electropolished Al-Cu alloy tips for atom probe tomography [35]. The solubility of Cu in Al is high [36–38], so the Cu enriched zone is likely formed by Cu atoms diffusing into the matrix from the surface layer in the time between electropolishing and characterization.

4.2. Cu layer – Crystal structure of and influence on TEM

The structure of the Cu layer is consistent with the θ'–Al$_2$Cu structure interfaced with Al, as reported earlier [23,24]. The orientation relationship is $(011)_{Al} \parallel (021)_{\theta'}$ and $[100]_{Al} \parallel [100]_{\theta'}$, with a $(011)_{Al} \parallel (021)_{\theta'}$ interface plane, which is one out of many possible orientation relationships [24]. According to the well-established θ' structure from Silcock [39], all the columns in Fig. 4c should have the same intensity. Instead, columns from every third $(011)_{\theta'}$ plane are more intense, so modifications to the structure are required. The θ' structure is known to exhibit stacking faults, interstitials and other kinds of reordering to e.g. accommodate misfit or ease its nucleation [15,40,41], so a thin surface layer of θ' having a different structure than θ' precipitates inside the Al matrix is not unexpected.

A suggested (unrelaxed) model of the layer with a modified θ' structure is shown in Fig. 7a. To account for the more intense columns observed in the $\left[0\overline{1}1\right]_{Al/\theta'}$ projection, every interstitial position was filled in every third $(011)_{\theta'}$ plane. This produces an orthorhombic superstructure with a $0.405 \times 0.707 \times 0.994$ nm unit cell. The 0.994 nm periodicity along the $\left[0\overline{2}1\right]_{\theta'}$ direction, corresponding to $3 \times d^{\theta'}_{(001)}$, is an excellent fit to the lattice modulation spacing along $\left[0\overline{1}1\right]_{Al}$ observed in Fig. 2d and the inset of Fig. 5, which corresponds to $7 \times d_{\left(0\overline{2}2\right)}^{Al} = 1.002$
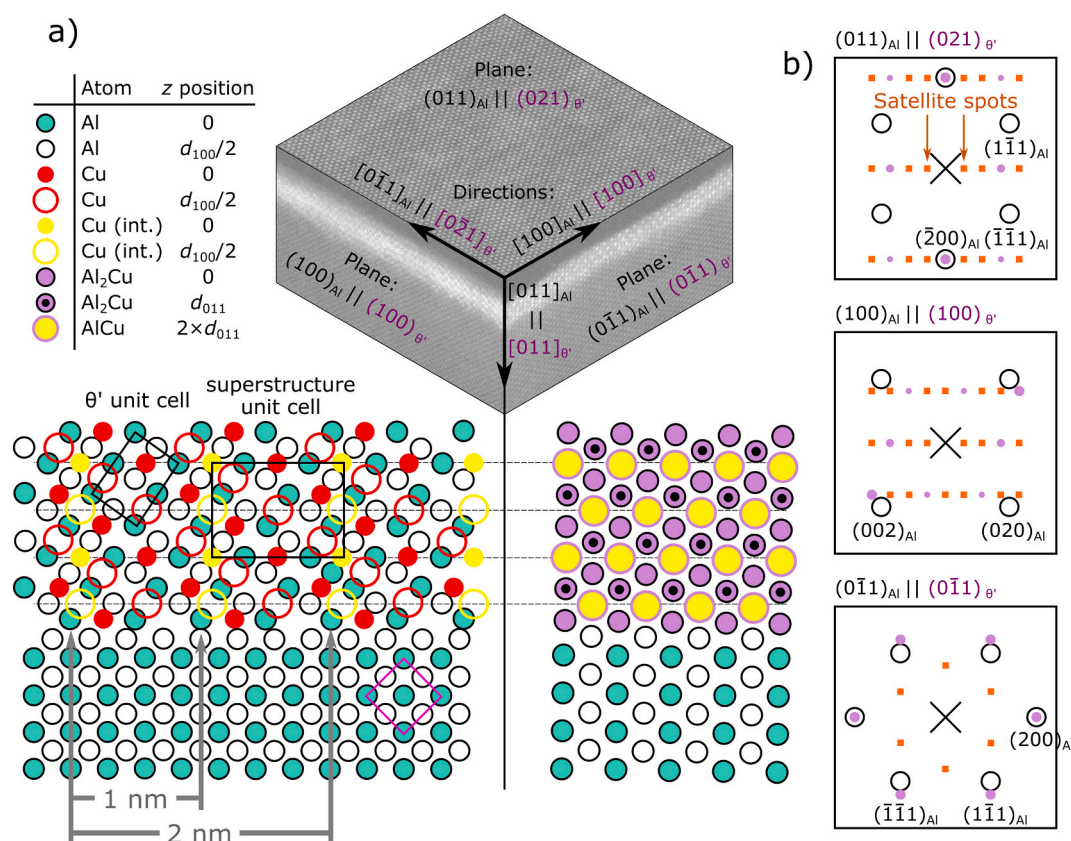
Fig. 7. a) Suggested (unrelaxed) atomic model of the Cu layer, based on the θ' structure with interstitial (int.) Cu. The atom heights (z) are measured in units of θ' plane spacings. The $[100]_{Al}$ and $\left[0\bar{1}1\right]_{Al}$ projections are shown. b) Simulated diffraction patterns from all three projections, with Al spots as black rings, θ' (Silcock model) spots as pink circles and additional θ' superstructure spots as orange squares. (For interpretation of the references to colour in this figure legend, the reader is referred to the web version of this article.)

nm. Meanwhile, the atomic model shows that the repeat distance of the interface is 2 nm, which fits well with the dislocation spacing found in Fig. 5.

In Fig. 7b, simulated kinematic diffraction patterns of our proposed structure are shown. These can be compared with the experimental Fourier transforms in Fig. 4b,d. While the $\left(0\bar{1}1\right)_{Al}$ projection is correct, the experimental $(100)_{Al}$ Fourier transform is missing several spots. This could have many reasons, such as overlap between different θ' domains that causes spot extinction, or simply inaccuracies in the model. In the $(011)_{Al}$ projection (through the electropolished surface), many spots are again expected, but only two satellite spots around each Al spot is visible in Fig. 2e-f due to the much stronger electron interactions with Al than with the thin θ' layers. While our atomic model does not necessarily represent the structure of the Cu layer perfectly, it is sufficient for explaining the artifacts observed in STEM images and diffraction patterns from electropolished specimens. We therefore propose that the superstructure is responsible for the lattice modulation and the satellite spots in $[011]_{Al}$ projected diffraction patterns (Fig. 2d-f).

This leaves the forbidden {110} diffraction spots seen in the [001] projection (Fig. 2b-c). These can originate from a θ' layer with the orientation relationship $(001)_{Al}\|(001)_{\theta'}$ and $[100]_{Al}\|[100]_{\theta'}$ [24]. As shown in Fig. 6c, the spots can also be produced by the Cu enriched zone below the θ' layer. A "checkerboard" $L1_0$ ordering of Cu on the fcc-Al matrix can explain the presence of these spots.

Density/concentration modulations have been reported in the Al matrix for Al-Mg alloys [20], Al-Mg-Si alloys [29] and Al-Zn-Mg alloys [42]. In the Al-Mg case, the alloys had a very high concentration of Mg, and the periodicities of the modulations changed with heat treatment, which indicates that they were a feature of the bulk lattice. In the other

two cases, the periodicity was 1.0 nm and 1.2 nm, similar to the periodicity measured in Fig. 2d and in the same lattice direction. Therefore, the reported modulations probably originated from superstructures in a θ' layer rather than a spinodal decomposition in the Al matrix.

From the imaging and chemical analysis done on the electropolished specimen of alloy 2, we can estimate the relative thicknesses of the layers that the electron beam goes through. For the best (S)TEM image quality, a thin specimen is required, and it is not unusual to find locations where an electropolished specimen has a thickness of 30 nm or lower. A volume of total thickness 30 nm will consist of 17% aluminium oxide, 10% θ' phase, 33% Cu-enriched matrix, and 40% unaffected matrix. A schematic of this is shown in Fig. 8.

When diffraction spots or peaks in a spectrum are observed, the TEM operator will naturally assume that they represent a feature of the material being studied. Our ToF-SIMS measurement and cross-sectional TEM study have shown that the aluminium surface is greatly affected
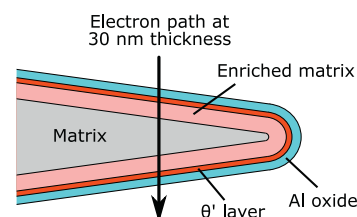

Fig. 8. Schematic of an electropolished TEM specimen viewed in cross-section, using the measured layer thicknesses from alloy 2. The wedge angle is greatly exaggerated.

by the sample preparation, which must be kept in mind in both chemical and structural analysis. For instance, the {110} forbidden spots can originate both from a θ' layer and a $L1_0$ ordering of Cu or other elements in the matrix, which may or may not be an actual feature of the bulk material.

The θ' layer can conceivably also reduce image quality or introduce artifacts in low-voltage high-resolution scanning electron microscopy and in electron backscattered diffraction, where surface quality is important, and electropolished specimens are typically used.

4.3. Cu layer – What to do with it?

The IPCMS analysis of electrolytes in Table 2 indicates that the electrolyte must be protected from contaminants on all surfaces it touches to avoid transferring the contaminants to TEM specimens. Improving the purity of the electrolyte solution can conceivably mitigate the Cu layer problem as well as reducing contamination of Ca, Na, and hydrocarbons, which were all measured using ToF-SIMS on a specimen prepared using a fresh electrolyte. It is uncertain whether exchanging the nitric acid/methanol mixture for another electrolyte would help. For instance, some common electrolytes use perchloric acid, which also dissolves Cu well [43] and would lead to the same problems. Rinsing everything the electrolyte comes into contact with using distilled/deionized water instead of tap water is an obvious improvement. A diluted acid may be applied first to remove any deposited metal ions. Using an individual electrolyte exclusively for Cu-free aluminium alloys might also be worthwhile.

Other preparation methods can be considered, although none give as large, evenly thin areas as electropolishing. Broad-beam Ar^+ ion milling gives a much higher wedge angle than electropolishing (typically 8° compared to around 1°) and has its own problems with surface roughness and redeposition of elements onto the specimen. FIB with a Ga^+ beam introduces Ga into the specimen, which might pose a larger problem than Cu, as it segregates to all defects, although cryo-FIB seems to mitigate this problem [44]. Xe^+ (plasma) FIB is an emerging option that avoids ion implantation. Ultramicrotomy is unsuitable as it introduces too much mechanical deformation to be useful for a ductile metal such as aluminium. Ultimately, electropolishing is fast and cheap, and is therefore not easily replaced as a high-throughput technique for preparing high-quality specimens.

It remains to ask whether aluminium with super-thin epitaxial θ' layers can have any applications in addition to being a nuisance in characterization. Does it have potential as an easily manufactured functional material? Depending on the electronic properties of the θ' phase, junctions could be created that might be useful for optical or electronic applications, or for growth of additional crystalline layers compatible with the θ' structure.

5. Conclusion

A Cu-rich layer with θ'–Al_2Cu structure is shown to form on the surfaces of electropolished aluminium alloy specimens. The alloy itself does not need to contain Cu for this to occur, as any Cu picked up by the electrolyte solution can be deposited on the Al surface. It is unclear whether selective dealloying or deposition from the electrolyte is the most important mechanism for the Cu layer to form. Further, Cu atoms can diffuse into the Al matrix from the θ' layer, creating a Cu enriched zone.

Crystallographic artifacts are observed in transmission electron microscopy, in imaging and diffraction modes, due to the Cu enrichment on the surface. With the specimen surface normal to (and electron beam parallel to) the $[001]_{Al}$ direction, forbidden $\{110\}_{Al}$ diffraction spots can result from both the θ' layer itself and the Cu enriched zone. With the surface normal parallel to $[110]_{Al}$, a θ' superstructure can produce satellite diffraction spots indicating a 1.0 nm periodicity in the $\left[0\bar{1}1\right]_{Al}$

direction. These phenomena are observed both in diffraction and ADF-STEM imaging. Other surface planes and θ'–Al orientation relationships may produce different artifact diffraction spots and image features.

Knowledge of possible Cu enrichment on electropolished aluminium surfaces is important in order to correctly interpret images and diffraction patterns obtained in TEM.

Data availability

The raw data used to produce the figures and tables in this paper are available at Mendeley Data: doi:10.17632/5ks69cckkp.1

Declaration of Competing Interest

The authors declare that they have no known competing financial interests or personal relationships that could have appeared to influence the work reported in this paper.

References

[1] R. Berthier, N. Bernier, D. Cooper, C. Sabbione, F. Hippert, P. Noé, In situ observation of the impact of surface oxidation on the crystallization mechanism of GeTe phase-change thin films by scanning transmission electron microscopy, J. Appl. Phys. 122 (11) (2017) 115304.

[2] L. Nguyen, T. Hashimoto, D.N. Zakharov, E.A. Stach, A.P. Rooney, B. Berkels, G. E. Thompson, S.J. Haigh, T.L. Burnett, Atomic-scale insights into the oxidation of aluminum, ACS Appl. Mater. Interfaces 10 (3) (2018) 2230–2235.

[3] L. Zou, W.A. Saidi, Y. Lei, Z. Liu, J. Li, L. Li, Q. Zhu, D. Zakharov, E.A. Stach, J. C. Yang, G. Wang, G. Zhou, Segregation induced order-disorder transition in Cu (Au) surface alloys, Acta Mater. 154 (2018) 220–227.

[4] S.P. Cooil, E.A. Mørtsell, F. Mazzola, M. Jorge, S. Wenner, M.T. Edmonds, L. Thomsen, H.W. Klemm, G. Peschel, A. Fuhrich, M. Prieto, T. Schmidt, J.A. Miwa, R. Holmestad, J.W. Wells, Thermal migration of alloying agents in aluminium, Mat. Res. Express 3 (11) (2016) 116501.

[5] Y.J. Xiao, F.Z. Fang, Z.W. Xu, W. Wu, X.C. Shen, The study of Ga+ FIB implanting crystal silicon and subsequent annealing, Nucl. Instrum. Methods Phys. Res., Sect. B 307 (2013) 253–256.

[6] S. Rubanov, A. Suvorova, Ion implantation in diamond using 30keV Ga+ focused ion beam, Diam. Relat. Mater. 20 (8) (2011) 1160–1164.

[7] M.J. Süess, E. Mueller, R. Wepf, Minimization of amorphous layer in Ar+ ion milling for UHR-EM, Ultramicroscopy 111 (8) (2011) 1224–1232.

[8] J.S. Luo, C.S. Sung, W.S. Hsu, L.Y. Huang, J.D. Russell, Electron beam induced carbon deposition using hydrocarbon contamination for XTEM analysis, Microelectron. Reliab. 50 (9) (2010) 1446–1450.

[9] C.M. McGilvery, A.E. Goode, M.S.P. Shaffer, D.W. McComb, Contamination of holey/lacey carbon films in STEM, Micron 43 (2) (2012) 450–455.

[10] D.R.G. Mitchell, Contamination mitigation strategies for scanning transmission electron microscopy, Micron 73 (2015) 36–46.

[11] N. Ünlü, Preparation of high quality Al TEM specimens via a double-jet electropolishing technique, Mater. Charact. 59 (5) (2008) 547–553.

[12] G. Yang, B. Wang, K. Tawfiq, H. Wei, S. Zhou, G. Chen, Electropolishing of surfaces: theory and applications, Surf. Eng. 33 (2) (2017) 149–166.

[13] H.M. Tomlinson, An electro-polishing technique for the preparation of metal specimens for transmission electron microscopy, Philos. Mag. 3 (32) (1958) 867–871.

[14] S.J. Andersen, C.D. Marioara, J. Friis, S. Wenner, R. Holmestad, Precipitates in aluminium alloys, Adv. Phys. X 3 (1) (2018) 1479984.

[15] L. Bourgeois, Y. Zhang, Z. Zhang, Y. Chen, N.V. Medhekar, Transforming solid-state precipitates via excess vacancies, Nat. Commun. 11 (1) (2020) 1248.

[16] S.C. Wang, M.J. Starink, Precipitates and intermetallic phases in precipitation hardening Al–Cu–Mg–(Li) based alloys, Int. Mater. Rev. 50 (4) (2005) 193–215.

[17] K. Matsuda, Y. Sakaguchi, Y. Miyata, Y. Uetani, T. Sato, A. Kamio, S. Ikeno, Precipitation sequence of various kinds of metastable phases in Al-1.0mass% Mg2Si-0.4mass% Si alloy, J. Mater. Sci. 35 (1) (2000) 179–189.

[18] L. Stemper, M.A. Tunes, P. Oberhauser, P.J. Uggowitzer, S. Pogatscher, Age-hardening response of AlMgZn alloys with Cu and Ag additions, Acta Mater. 195 (2020) 541–554.

[19] J. Banhart, C.S.T. Chang, Z. Liang, N. Wanderka, M.D.H. Lay, A.J. Hill, Natural aging in Al-mg-Si alloys – a process of unexpected complexity, Adv. Eng. Mater. 12 (7) (2010) 559–571.

[20] T. Sato, Y. Kojima, T. Takahashi, Modulated structures and GP zones in Al-mg alloys, Metall. Trans. A. 13 (8) (1982) 1373–1378.

[21] L. Kovarik, S.A. Court, H.L. Fraser, M.J. Mills, GPB zones and composite GPB/GPBII zones in Al–Cu–Mg alloys, Acta Mater. 56 (17) (2008) 4804–4815.

[22] J.Z. Liu, J.H. Chen, D.W. Yuan, C.L. Wu, J. Zhu, Z.Y. Cheng, Fine precipitation scenarios of AlZnMg(cu) alloys revealed by advanced atomic-resolution electron microscopy study part I: structure determination of the precipitates in AlZnMg(cu) alloys, Mater. Charact. 99 (2015) 277–286.

[23] Z. Wang, K. Lv, J.K. Zheng, B. Chen, Atomic-scale characterization of interfaces between 2A70 aluminum alloy matrix and Cu-enriched layer after electropolishing, Mater. Charact. 150 (2019) 150–154.

[24] T. Hashimoto, X. Zhou, P. Skeldon, G.E. Thompson, Structure of the copper–enriched layer introduced by anodic oxidation of copper-containing aluminium alloy, Electrochim. Acta 179 (2015) 394–401.

[25] S. Kumari, S. Wenner, J.C. Walmsley, O. Lunder, K. Nisancioglu, Copper enriched by dealloying as external cathode in intergranular corrosion of aluminium alloy AA6005, Corros. Sci. 158 (2019) 108090.

[26] T. Sritharan, H. Li, Influence of titanium to boron ratio on the ability to grain refine aluminium-silicon alloys, J. Mater. Process. Technol. 63 (1) (1997) 585–589.

[27] I.S. Molchan, G.E. Thompson, P. Skeldon, N. Trigoulet, P. Chapon, A. Tempez, J. Malherbe, L. Lobo Revilla, N. Bordel, P. Belenguer, T. Nelis, A. Zahri, L. Therese, P. Guillot, M. Ganciu, J. Michler, M. Hohl, The concept of plasma cleaning in glow discharge spectrometry, J. Anal. At. Spectrom. 24 (6) (2009) 734–741.

[28] K. Shimizu, H. Habazaki, P. Skeldon, G.E. Thompson, G.C. Wood, GDOES depth profiling analysis of a thin surface film on aluminium, Surf. Interface Anal. 27 (11) (1999) 998–1002.

[29] S.J.A.C.D. Marioara, J. Friis, O. Engler, Y. Aruga, The Nature of Solute Clusters and GP-Zones in the Al-Mg-Si System, in: 16th International Conference on Aluminum Alloys, Canadian Institute of Mining, Metallurgy & Petroleum, 2018.

[30] K. Matsuda, A. Kawai, K. Watanabe, S. Lee, C.D. Marioara, S. Wenner, K. Nishimura, T. Matsuzaki, N. Nunomura, T. Sato, R. Holmestad, S. Ikeno, Extra

Electron diffraction spots caused by fine precipitates formed at the early stage of aging in Al-Mg-X (X=Si, Ge, Zn)-Cu lloys, Mater. Trans. 58 (2) (2017) 167–175.

[31] J.P. Ngantcha, M. Gerland, Y. Kihn, A. Rivière, Correlation between microstructure and mechanical spectroscopy of a Cu-Cu2 O alloy between 290 K and 873 K, Eur. Phys. J. Appl. Phys. 29 (1) (2005) 83–89.

[32] T.H. Merkel, H.-J. Groß, W. Werner, T. Dahlke, S. Reicherter, G. Beuchle, S. H. Eberle, Copper corrosion by-product release in long-term stagnation experiments, Water Res. 36 (6) (2002) 1547–1555.

[33] E.A. Travnicek, J.H. Weber, Continuous dissolution of copper by nitric acid, J. Phys. Chem. 65 (2) (1961) 235–240.

[34] N. Sallee, M. Cromer, O. Vittori, Electroplating of copper on aluminium with direct and pulsed currents, Can. Metall. Q. 33 (2) (1994) 155–162.

[35] F. Danoix, M.K. Miller, A. Bigot, Analysis conditions of an industrial Al–Mg–Si alloy by conventional and 3D atom probes, Ultramicroscopy 89 (1) (2001) 177–188.

[36] E.T. George, D.S. MacKenzie, Handbook of Aluminum, Physical Metallurgy and Processes, Marcel Dekker Inc., New York, 2003.

[37] I. Polmear, D. StJohn, J.-F. Nie, M. Qian, 2 - Physical metallurgy of Aluminium alloys, in: I. Polmear, D. StJohn, J.-F. Nie, M. Qian (Eds.), Light Alloys, Fifth edition, Butterworth-Heinemann, Boston, 2017, pp. 31–107.

[38] O. Zobac, A. Kroupa, A. Zemanova, K.W. Richter, Experimental description of the Al-Cu binary phase diagram, Metall. Mater. Trans. A 50 (8) (2019) 3805–3815.

[39] J.M. Silcock, T.J. Heal, H.K. Hardy, Structural ageing characteristics of binary aluminium-copper alloys, J. Inst. Met. 82 (1954) 239.

[40] S. Wenner, J. Friis, C.D. Marioara, S.J. Andersen, R. Holmestad, Structural modifications and electron beam damage in aluminium alloy precipitate θ'–AL2, Philos. Mag. 95 (31) (2015) 3524–3534.

[41] L. Bourgeois, C. Dwyer, M. Weyland, J.-F. Nie, B.C. Muddle, Structure and energetics of the coherent interface between the θ' precipitate phase and aluminium in Al–cu, Acta Mater. 59 (18) (2011) 7043–7050.

[42] K. Shen, Z.M. Yin, T. Wang, On spinodal decomposition in ageing 7055 aluminum alloys, Mater. Sci. Eng. A 477 (1) (2008) 395–398.

[43] A.J. Read, Dissolution of copper in weakly acidic solutions, J. Phys. Chem. 76 (24) (1972) 3656–3663.

[44] L. Lilensten, B. Gault, New approach for FIB-preparation of atom probe specimens for aluminum alloys, PLoS One 15 (4) (2020), e0231179.